Examining the Effects of Nitrogen-doped Carbon Coating on Zinc Vanadate Nanoflowers Towards High Performance Lithium Anode

Cao, Huili; Zheng, Zhiyong; Meng, Jie; Xiao, Xinxin; Norby, Poul; Mossin, Susanne

Published in:
Electrochimica Acta

Link to article, DOI:
10.1016/j.electacta.2020.136791

Publication date:
2020

Document Version
Peer reviewed version

Examining the Effects of Nitrogen-doped Carbon Coating on Zinc Vanadate Nanoflowers Towards High Performance Lithium Anode

Huili Cao[a], Zhiyong Zheng[a], Jie Meng[a], Xinxin Xiao[a], Poul Norby[b] and Susanne Mossin[a*]*

[a]Department of Chemistry, Technical University of Denmark, 2800 Kgs. Lyngby, Denmark

[b]Department of Energy Conversion and Storage, Technical University of Denmark, 2800 Kgs. Lyngby, Denmark

Corresponding authors: hucao@kemi.dtu.dk (Huili Cao); slmo@kemi.dtu.dk (Susanne Mossin)

Abstract: Coating transition metal oxides with nitrogen-doped carbon is an efficient way to enhance lithium-ion battery performance by improving the conductivity and stability of the electrodes. So far, little attention has been paid to how the calcination process affects bimetallic oxides, such as zinc vanadate, with regards to the oxidation state of the metal, the zinc/vanadium ratio and the specific surface area. In this work, we report nitrogen-doped carbon coated zinc vanadate nanoflowers (particle size: 10 nm; coating layer thickness: 20 nm) with a high specific surface area (115 m^2 g^{-1}) through a facile method. High-angle annular dark-field scanning transmission electron microscopy, X-ray diffraction and electron paramagnetic resonance spectroscopy reveal that V^{5+} from the precipitated $Zn_3(OH)_2(V_2O_7)(H_2O)_2$ is largely converted to V^{3+} in ZnV_2O_4. A vanadium loss of about 9% during calcination lead to increased Zn/V ratio and formation of ZnO. When applied as anode in a lithium-ion battery, the as-prepared ZnV_2O_4/ZnO@N doped C exhibits a considerable reversible specific capacity of 620 mAh g^{-1} at a current density of 0.1 A g^{-1} after 50 cycles, very close to the theoretical capacity (651 mAh g^{-1}) and considerably higher than the non-coated counterpart (306 mAh g^{-1}). The material is stable during extended cycling (200 cycles at 0.5 A g^{-1}). In-depth electrochemical analysis including three-electrode system testing shows that the carbon shell is crucial in maintaining the structure stability and enhancing the capacity of the active material.

Keywords: Nitrogen-doped carbon, oxidation state, zinc vanadate, anode, lithium-ion battery

1. Introduction

In recent years, transition metal oxides (TMOs) and carbon composites in core-shell structures have been used in a wide range of fields, including electromagnetic wave absorption,[1] sensors,[2] supercapacitors[3] and lithium-ion batteries (LIBs)[4-5]. The advantages are the low density and high conductivity of the carbon layer and the large fraction of void space. In a typical synthesis, the metal oxides are fabricated first in a certain morphology and then coated with a carbon layer to form a core-shell structure. The carbon shell can come from various sources: glucose,[6] starch,[7] polydopamine,[8] metal-organic frameworks,[9] pyrrole,[10] acrylonitrile[11], and pyridine.[12] Among them, starch is very attractive given its wide availability, non-toxicity and low-cost. The large amounts of hydroxyl groups in starch can coordinate well with metal ions, allowing good dispersion and well controlled size and shape of TMO nanoparticles. In order to improve the starch carbon properties further, the doping method play an important role.[13-16] Various doping strategies has been put up by different research groups; this includes doping with metal ions,[17-19] B,[20] and N[21-24]. Polydopamine,[25-26] is a biomimetic adhesive polymer that can easily coat on material surfaces by self-polymerization in aqueous media. Additionally, calcination of polydopamine results in a nitrogen-doped carbon layer with high electrical conductivity.[27-30]

For use as electrode material of LIB, commercial anodes are mainly relying on carbon-based materials, such as graphite, with a theoretical capacity of 372 mAh g^{-1}. There is a potential safety issue when using carbon-based anodes since lithium insertion primarily occurs at a low voltage of about 0.1 V vs. Li/Li^+,[31] which can lead to an internal short circuit due to the formation of lithium dendrites.[32] An alternative anode material is spinel lithium titanate ($Li_4Ti_5O_{12}$, LTO), exhibiting a high insertion potential about 1.55 V vs. Li/Li^+ for charge and discharge.[33-34] However, LTO suffers from a poor electronic conductivity and a limited theoretical capacity of 175 mAh g^{-1}.[35]

Zinc vanadium oxide materials are among the most promising anode candidates, possessing a similar insertion potential to spinel LTO and a much higher theoretical capacity over 500 mAh g^{-1}. Zinc vanadate exists in several crystal forms including a spinel-type. It can be converted to composite materials with both conversion-type (zinc vanadate) and alloying material (Zn). Alloying materials

exhibit higher gravimetric capacity compared to conversion-type materials, and suffers from more serious volumetric expansion during Li^+ uptake.[36-37] Therefore, the mixed conversion type and alloying type materials are applied in mixed-valence TMOs to give an excellent electrochemical performance. The complex chemical composition allows interfacial and synergistic effects between the multiple metal species.[38] For example, Yin et al.[39] synthesized hollow $Zn_3V_2O_8$ nanocages by a solvothermal method showing a capacity of 1400 mAh g^{-1} at a current density of 100 mA g^{-1} after 80 cycles. Luo et al.[40] employed electrospinning to fabricate one-dimensional $Zn_2V_2O_7$ nanofibers with a capacity of 700 mAh g^{-1} after 100 cycles at a current density of 50 mA g^{-1}. It is hypothesized that carbon coating is effective to improve the electronic conductivity while maintaining a stable morphology of zinc vanadate.

Similar to some other TMOs, zinc vanadate is expected to be reduced to a lower oxidation state due to the presence of carbon during the calcination process. For example, Wang et al.[41] calcinated porous Mn_2O_3 microspheres coated with polypyrrole and identified the product as MnO/NC by XRD. Similarly, FeOOH nanorods[42], Ni/C composites[43], peapod-like V_2O_3 nanorods[44], and VO_2-carbon composites[45] with carbon coatings were derived from metal oxide precursors with higher oxidation states. Bimetallic oxides such as core-shell $Zn_3V_3O_8$/C composite microspheres[46] were obtained from PVP encapsulated $Zn_3V_2O_7(OH)_2$, where V^{5+} was reduced to V^{4+} and V^{3+}. These examples clearly demonstrate that carbon coating induces reduction of the metal. It is important to understand the chemical composition of the electrode completely, because it will not only help us to estimate the number of electrons that can be transferred, but also to identify the chemical reactions during the charge and discharge process. Analysis of the reduction process is often limited to XRD and XPS, which might not be suitable for nano-scaled samples with broad XRD peaks or on particles encapsulated in thick shells with week XPS signals. It's noteworthy, but not widely recognized, that the bimetallic oxide zinc vanadate might also experience a zinc to vanadium ratio change during calcination[46].

Herein, we report a facile method to synthesize nitrogen-doped (N-doped) carbon-coated porous flower-like zinc vanadate by a simple direct precipitation at room temperature and calcination in an argon atmosphere. To investigate the effects of the calcination process on the ratio of metal ions and the vanadium oxidation state, ICP-OES, EPR and HADDF-EELS are applied to obtain the concentration

of zinc and vanadium in the as-prepared products, and the prevalent oxidation state of vanadium after the coating process. The materials are applied as the anode of LIBs revealing that the core-shell carbon-coated zinc vanadate with a high specific surface area (115 m^2 g^{-1}) exhibits a high stable specific capacity of 404 mAh g^{-1} at 500 mA g^{-1} after 250 cycles. We hypothesize that the porous structure is well suited to accommodate the volume expansion and extraction during the electrochemical process. A three-electrode system is applied to study the contribution of the anode to the impedance of the whole cell.

2. Experimental

2.1 Chemicals

Zinc acetate dihydrate ($Zn(CH_3COO)_2 \cdot 2H_2O$, 99.0%, CAS:5970-45-6), ammonium metavanadate (NH_4VO_3, 99.0%, CAS:7803-55-6), and carbon black (99.9%, CAS: 1333-86-4) were bought from Alfa Aesar. Starch ($(C_6H_{10}O_5)_n$, CAS:9005-25-8), poly(vinylidene fluoride) (PVDF, $(CH_2CF_2)_n$, average M_w ~534.000), dopamine hydrochloride (2-(3,4-dihydroxyphenyl)ethylamine hydrochloride, $C_8H_{11}NO_2 \cdot HCl$), tris base (2-amino-2-hydroxymethyl-1,3-propanediol, tris(hydroxymethyl)aminomethane, $C_4H_{11}NO_3$, 99.9%) and 1-methyl-2-pyrrolidinone (C_5H_8NO, NMP, 99.5%) were purchased from Sigma-Aldrich, Denmark.

2.2 Synthesis of $Zn_3V_2O_8$@N-doped carbon flowers

In a typical synthesis, 1 mmol NH_4VO_3 was dissolved in 20 mL Milli-Q water to form solution A at 80 ^oC. 1.5 mmol $Zn(CH_3COO)_2 \cdot 2H_2O$ and 0.5g starch were dissolved in 30 mL Milli-Q water to form solution B at room temperature (RT). Solution A was added into solution B and stirred for 1 h at RT to form the precursor in solid form (ZnVS). After filtration and washing with Milli-Q water and ethanol several times, the precursor was stirred in 80 mL tris-buffer with a pH of 8.5 (about 10 mM), into which 45 mg dopamine was added. After stirring overnight, the polydopamine (PDA) coated precursor was isolated by filtration and washed with water and ethanol. The PDA coated precursor was calcinated at 550 ^oC for 2 h in Ar atmosphere at a ramping rate of 5 ^oC min^{-1} to obtain ZnVC. For comparison, the pure precursor was also calcined in air (ZnVair) and Ar (ZnVAr) at the same temperature.

2.3 Material characterization

X-ray powder diffraction patterns (XRD) of various samples were recorded using an Image Plate Huber G670 Guinier diffractometer (Cu Kα1 radiation, transmission mode). Field emission scanning electron microscopy (SEM) and energy-dispersive X-ray spectroscopy (EDX) characterizations were carried out on a FEI Quanta FEG 200 ESEM. Transmission electron microscopy (TEM) investigations and selected area electron diffraction (SAED) were studied by a FEI Tenai T20 operated at 200 kV equipped with a CCD camera. The high-angle annular dark-field scanning transmission electron microscopy (HAADF-STEM) images and electron energy loss spectroscopy (EELS) were obtained with a FEI Titan Analytical 80-300ST TEM at 300 kV. X-ray photoelectron spectroscopy (XPS) was tested with a Thermo Scientific K-alpha spectrometer using Al Kα radiation. Electron paramagnetic resonance (EPR) spectra were collected on an EMX X-band continuous-wave (CW) EPR spectrometer with an ER 4102ST cavity at RT. Thermal gravimetric and differential thermal analysis (TGA, DTA) was measured in air with a ramping rate of 5 or 10 ^{o}C min^{-1} and heated up to 700 ^{o}C. Textural properties were determined via nitrogen sorption at -200 ^{o}C using a conventional volumetric technique on an ASAP 2020. The surface area was calculated using the Brunauer-Emmett-Teller (BET) method based on the adsorption branch of nitrogen adsorption/desorption isotherms. The elemental composition of the sample was determined via inductively coupled plasma-optical emission spectroscopy (ICP-OES) analysis on a Perkin Elmer 3000 DV analyzer.

2.4 Electrochemical measurements

The active material, carbon black and poly(vinylidene fluoride) (PVDF) with a weight ratio of 8:1:1 were mixed in 1-methyl-2-pyrrolidinone (NMP) to form a homogenous slurry, which was then coated on a copper foil current collector and dried in a vacuum oven at 120 ^{o}C for 12h. The coated copper foil was punched into a circle with a diameter of 15 mm and used as the working electrode. The loading of the active material was determined to be about 1 mg cm^{-2}. Glass microfiber filters dried at 120 ^{o}C in a vacuum oven overnight were used as the separator. The tested cells were assembled in an argon glove box. A disc of fresh Li foil with a diameter of 15 mm was used as the combined counter-/reference electrode, with 1 M $LiPF_6$ in ethylene carbonate/dimethyl carbonate (EC: DMC = 1:1 by volume) as

the electrolyte. Galvanostatic testing of the cell was evaluated in a voltage range of 0.02-3.00 V at various current densities. Cyclic voltammetry (CV) was measured in the same potential range at a scan rate of 0.1 mV s^{-1} and electrochemical impedance spectroscopy (EIS) at the open-circuit voltage in a frequency range of 0.1 to 100k Hz were tested on either a Metrohm Autolab potentiostat or a Biologic Science Instrument VMP3.

3. Results and discussion

3.1 Morphology and structure characterization

The synthesis of N-doped carbon-coated zinc vanadate is illustrated in Figure 1. The precursor (ZnVS) precipitates directly by mixing solutions of the zinc and vanadium salts at RT in a flower-like morphology. The formation of his morphology is thought to take place through an Ostwald ripening process.[47] PDA coating is performed by simply adding dopamine into the tris-buffer (pH 8.5) suspension of ZnVS, undergoing spontaneous polymerization.[48] Zinc vanadate coated carbon composites (ZnVC) are obtained after the carbonization of PDA coated ZnVS. By calcination the ZnVS in air and Ar, the comparison samples ZnVair and ZnVAr can be obtained, respectively.

The detailed morphology and the structural features of the products were investigated by SEM and XRD. The as-obtained precursor ZnVS is well distributed and exhibits a uniformly flower-like structure with an average size of 500 nm, as shown in Figure S1. The higher magnification image (Figure 1a) shows that the flower is assembled by nanosheets with smooth surfaces. All the peaks of the precursor (ZnVS) can be indexed to $Zn_3(OH)_2(V_2O_7)\cdot 2H_2O$ (ICOD: 00-087-0417), in Figure 1b. A broad peak appears at around 10 to 20^o after PDA coating, indicating that the amorphous polymer dopamine is successfully introduced into the ZnVS.

When as-produced ZnVS is calcinated in air (to ZnVair), the smooth nanosheets of the flower shrink into nanoparticles in the same overall size (about 500 nm) as in ZnVS (Figure 1d). XRD patterns (Figure 1g) display the highly crystalline peaks corresponding to the orthorhombic crystal structure of $Zn_3V_2O_8$ (ICOD:00-034-0378). TEM is used at low magnification in order to estimate the average size of the nanoparticles, As shown in Figure S2a and b, the nanoparticles in ZnVair are well distributed with sizes

of about 100-300 nm. The high-resolution TEM (Figure S2c) recorded on the particles shows clear lattice fringes, and the calculated interplanar spacing is ca. 0.247 nm, assigned to the (311) plane of $Zn_3V_2O_8$.

ZnVAr is a black powder obtained by calcination of ZVS in an Ar atmosphere, the colour indicating carbonization of a remnant of starch in the precursor. ZnVAr maintains the flower morphology (Figure 2e). The surface of the ZnVAr flower is rougher than that of ZnVS. TEM images show a porous flake structure (Figure S2d and e), composed of nanoparticles with an average size of 10 nm. The lattice fringes on the nanoparticle (Figure S2f) indicate good crystallinity of the product. In the corresponding converted fast Fourier transform (FFT) pattern (inset of Figure S2f), it is determined that the diameter of the spot is ca. 3.96 1/nm, corresponding to an interplanar spacing of 0.253 nm. This is assigned to the (311) plane in the spinel structure of Zn_2VO_4 or ZnV_2O_4, which contains vanadium in lower oxidation states (V^{4+} or V^{3+}). It indicates that some of the vanadium has been reduced to a lower oxidation state by starch during calcination. Due to the small size of the nanoparticles, there are some broad peaks in the XRD patterns (Figure 1h). The main diffraction patterns at 30.0°, 35.4°, 56.9°, and 62.5° (2 theta) can be assigned to the (220), (311), (511), and (440) crystal planes of either Zn_2VO_4 (ICOD:01-073-1632) or ZnV_2O_4 (ICOD:01-075-0318). Peaks at 31.7°, 34.4°, and 36.2° correspond to the (010), (002) and (011) crystal planes of ZnO (ICOD: 00-001-1136).

Figure 1f shows that the ZnVC also maintains the flower structure of the precursor. The XRD result (Figure 1i) shows that ZnVC and ZnVAr primarily consists of the same crystal phase. A typical STEM image of the ZnVC flowers is given in Figure 2a, suggesting an uniform distribution of the samples. The carbon layer coats the flake uniformly to form a core-shell structure. The thickness of the layer is ca. 20 nm, with a porous inner core (of ca. 10 nm in diameter, see Figure 2b). The line scan EDS element analysis by HAADF-STEM in Figure 2c is used to confirm the core-shell element distribution. Zn, V, and O are the dominant elements at the centre of the flake and are uniformly distributed. The outside shell contains C and N. Thanks to the supporting carbon layer, the flake keeps integrity during the calcination process. The high-resolution TEM image of the ZnVC clearly shows the crystalline structure. By calculating the converted FFT spots (inset of Figure 2d), the lattice fringes (0.253 nm) again

correspond to Zn_2VO_4 or ZnV_2O_4. Raman spectroscopy (Figure S3) is applied to investigate the presence of carbon in ZnVAr and ZnVC. There are two peaks in the Raman spectrum at about 1340 and 1600 cm^{-1}, which can be assigned to amorphous carbon (D-band) and graphitic carbon (G-band), respectively.[49-50] This indicates the presence of carbon in both ZnVAr and ZnVC.

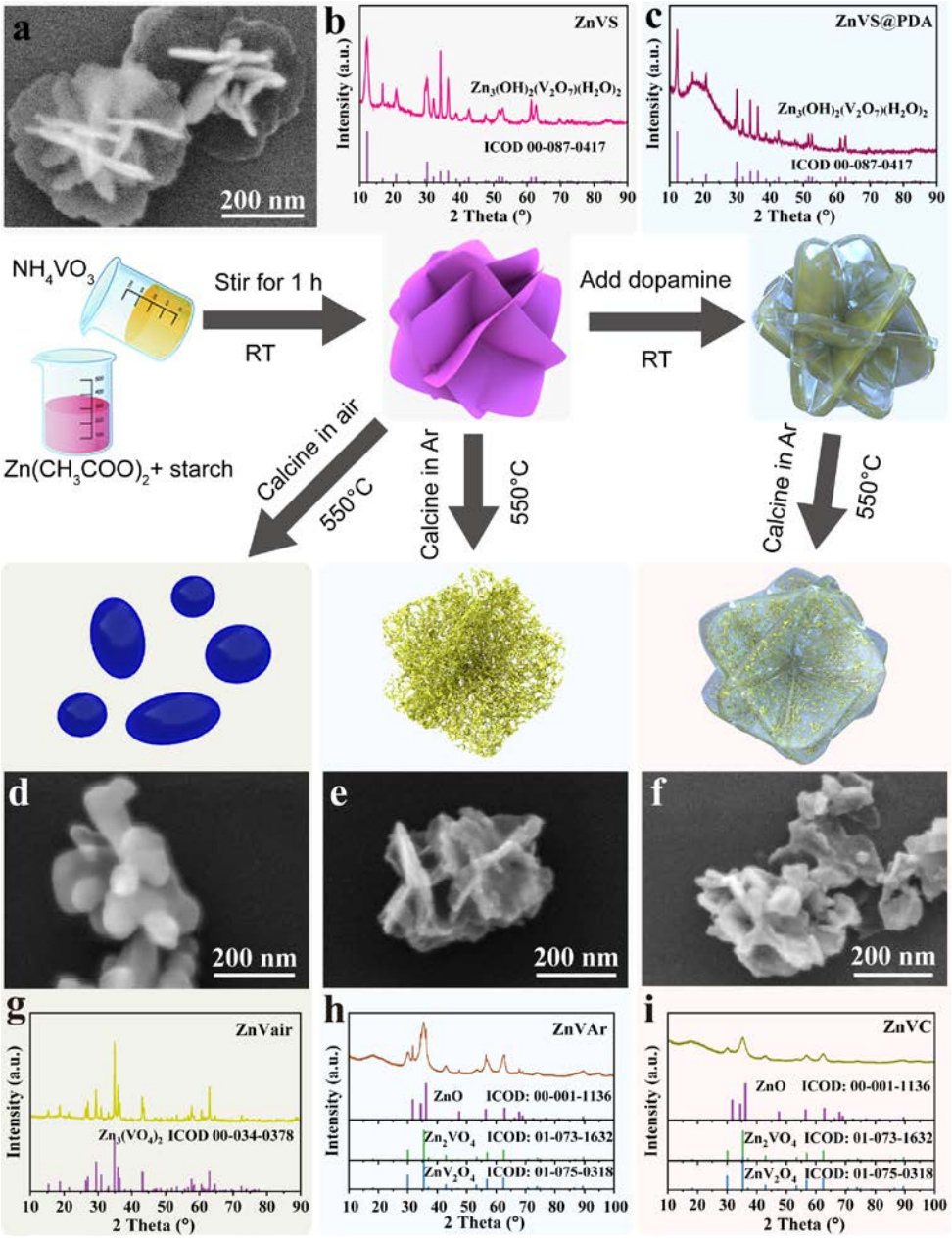

Figure 1. Schematic illustration of the three types of zinc vanadate synthesis process. SEM image and XRD patterns of precursor ZnVS (a) and (b), XRD pattern from ZnVS coated with dopamine (c); SEM images and XRD patterns of ZnVair (d) and (g), ZnVAr (e) and (h), and ZnVC (f) and (i).

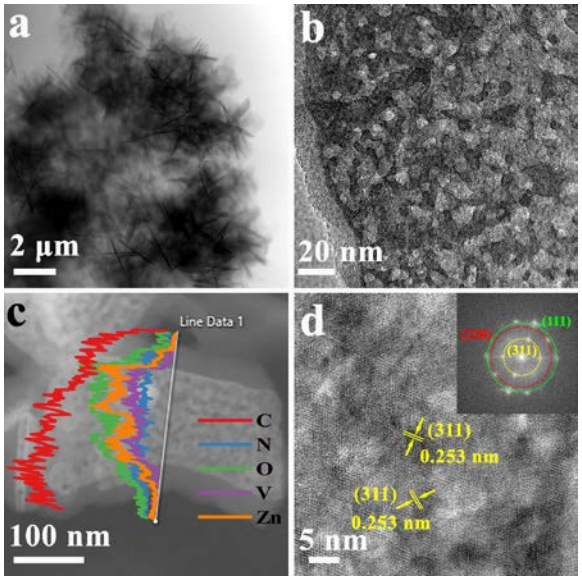

Figure 2. STEM images at low magnification (a); TEM image of the porous structure (b), HAADF image and linear scan EDS elemental analysis of core-shell ZnVC (c), and HRTEM image of ZnVC (d). Inset of (d) is the corresponding converted FFT spots.

3.2 The oxidation state of vanadium

Dopamine, a non-toxic and safe carbon source, can be easily polymerized and coated on the metal oxide surface and forms an N-doped carbon layer upon calcination. Vanadium in the component metal oxides will be reduced from +5 to lower oxidation states during the carbon coating process in an inert atmosphere like what is observed for both Mn-based oxides and Fe-based oxides.[51-52] The oxidation state of V after the calcination process is difficult to predict, in particular as a ternary metal oxide. The oxidation state of V in the spinel structure can not be determined by XRD due to the low crystallinity of the materials. XPS is thus applied to further investigate the products. As shown in Figure 3a, the precursor ZnVS contains Zn, V, C, and O. C might come from starch or carbon contamination. The sharp peaks at 1020.87 and 1043.67 eV are assigned to Zn 2p1/2 and Zn 2p3/2 from Zn^{2+},[53] with the small peaks between 527 and 512 eV assigned to V 2p. The same peaks can be observed in ZnVair, ZnVAr and ZnVC. There is an extra tiny peak in ZnVC at 399.37 eV which is assigned to N 1s, due to the dopamine carbon source. In the high-resolution XPS pattern of V 2p in Figure 3b, the peaks of ZnVAr and ZnVC are redshifted to lower binding energy position, indicating the reduction of vanadium during the calcination process.[54] The peak patterns are analyzed by fitting with Gaussian shapes, as shown in Figure S4. The main peaks observed for ZnVS at 517.2 and 524.4 eV originate from V^{5+} 2p3/2

and V^{5+} 2p1/2.[55] The sharp peaks in ZnVair are observed at the same position, indicating the presence of V^{5+}. Peaks assigned to V^{4+} can be observed as well at 515.9 and 522.7 eV. ZnVAr and ZnVC both show peaks that can be assigned to V 2p3/2 at about 515.8 eV, corresponding to V^{4+} and clear shoulders that show the presence of V^{3+}. Although XPS is employed successfully in some vanadium-based materials, in this particular case this method seems to be less useful due to the proximity of O1s. Besides, the relevant peak in a V_2O_3/carbon composite might also blue shift compared to the peak in pure V_2O_3. For example, Wu et al.[56] fabricated amorphous V_2O_3/C where the V 2p3/2 peak is located at 517.2 eV. We concluded that another approach is needed to confirm unequivocally the oxidation state of vanadium.

Electron energy loss spectroscopy (EELS) is commonly used to identify the oxidation state of transition metals in materials because the near edge features of the element are highly sensitive to the local valence electronic structures.[57] Figure 3c shows that the vanadium L edge of ZnVC and the L3 energy loss peak is located at 518.5 eV. It is still difficult to confirm the oxidation state of vanadium due to the use of different standards in various works.[58] Nevertheless, the oxidation state of vanadium in ZnVC could be limited to be either V^{3+} or V^{4+} according to the combination of all of the characterization efforts described above.

EPR spectroscopy is a very powerful method to identify V^{4+} species, due to its $3d^1$ electron configuration with an electron spin S=1/2. V^{5+} is diamagnetic and always EPR silent. Whereas V^{3+} is an integer spin system (S=1) that is not observed at RT in X-band EPR spectroscopy due to a high zero-field splitting, but it is possible to detect it by other types of EPR investigations. EPR is applied here to detect and quantify V^{4+}. The EPR spectra of ZnVS, ZnVair, ZnVAr, and ZnVC at RT are given in Figure 3d, confirming the presence of V^{4+} ions in all samples. It is recognized by the characteristic splitting pattern due to the interaction of the unpaired electron with the ^{51}V nuclei (natural abundance 100%) with a nuclear spin of I=7/2. The sharp central peak in ZnVAr and ZnVC confirms the presence of carbon residues and the broadening at the base of the sharp peak in ZnVC indicates the presence of N-doping (^{14}N has I=1). To quantify the amount of EPR active V^{4+} ions, the background-corrected spectra are integrated twice and compared to the double integral of reference samples consisting of $VOSO_4 \cdot 3H_2O$ diluted in K_2SO_4. The results are collected in Table 1. In ZnVS, ZnVair, and ZnVAr, the

concentration of V^{4+} correspond to less than 0.06% of the total vanadium content. The integration of ZnVC shows a relatively higher concentration of about 0.167%, but closer analysis of the spectra shows that most of the EPR signal is due to C and N-based radicals in the N-doped carbon shell. The amount of EPR active V^{4+} is comparable to the other samples.

Based on all data presented here, we suggest that the precursor ZnVS mainly contains V^{5+}, unchanged from the NH_4VO_3 starting material. ZnVair is obtained by calcination in air and is also confirmed to contain only V^{5+}. On the other hand, vanadium in ZnVAr and ZnVC is mainly reduced to V^{3+}, in a form of the spinel ZnV_2O_4. The main crystalline phases in ZnVAr and ZnVC are ZnV_2O_4 and ZnO.

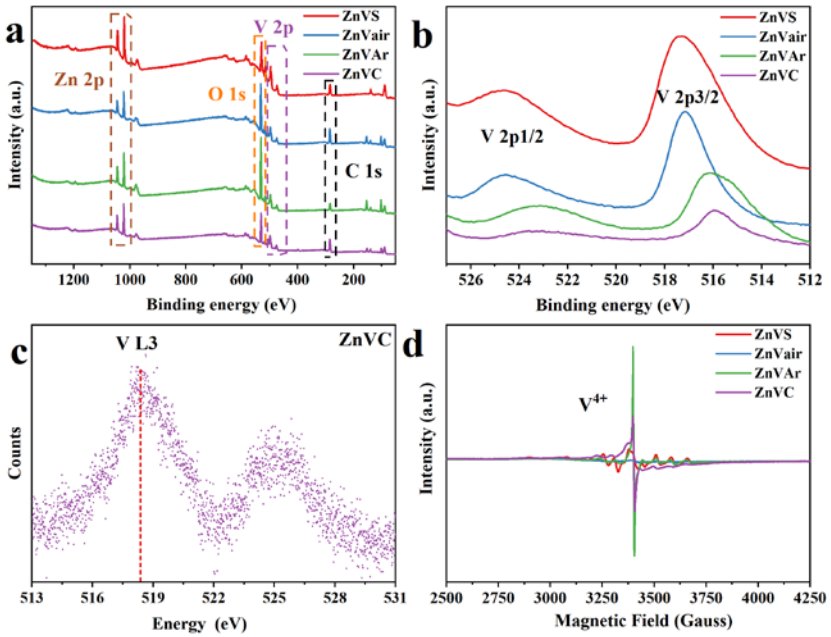

Figure 3. XPS survey spectra (a), and V 2p (b) of ZnVS, ZnVair, ZnVAr and ZnVC; EELS spectroscopy at vanadium L edge of ZnVC (c); and EPR spectra (d).

Table 1 *Percentage of V^{4+} obtained from EPR*

Sample	*ZnVS*	*ZnVair*	*ZnVAr*	*ZnVC*
Total Mass (ppm)	*22.28*	*23.29*	*24.95*	*19.89*
V^{4+}	*0.056%*	*0.025%*	*0.032%*[a]	*0.167%*[a]

[a]The majority of the EPR signal in ZnVAr and ZnVC is due to a C-centered radical

3.3 Loss of vanadium during calcination

It was reported in the literaturethat the ratio of Zn to V may change during synthesis.[46, 59] To confirm the composition of the obtained materials, the elemental analysis is performed by ICP analysis. All the

samples are dissolved by heating in 70% HNO_3 and then diluted to 3% HNO_3. The corresponding concentrations are calibrated using standard curves (Fig. S4a). The results are collected in the first two rows in Table 2. In the precursor ZnVS, Zn mass concentration is 34.26% and V ion mass concentration is 17.33%, giving a Zn/V ratio of 1.540 in accordance with the crystalline phase $Zn_3(OH)_2(V_2O_7)(H_2O)_2$ as suggested by XRD. For ZnVair, the calcination process has converted the hydroxide to oxide and removed crystal water. Thus, the Zn and V concentration increases to 47.13% and 23.72%, but the ratio is the same (1.547). The procedure performed during TGA in air will result in the loss of water and carbon (giving a weight loss) and the oxidation of all vanadium to V_2O_5 (giving the possibility of a weight gain). It is almost the same procedure that is performed in order to convert ZnVS to ZnVair. The TGA results for ZnVS, ZnVAr and ZnVC are found in Figure S5b-d. For ZnVS (Figure S5b) the residual mass is 68.80%. During the initial drying process, about 4.43% moisture is lost and the more relevant value to compare is 72.0%. A value of 73.58% is calculated from the ICP results under the assumption that the residual mass after the TGA experiment is only due to Zn^{2+}, V^{5+} and charge compensating O^{2-}, see the bottom row of Table 2. The TGA analysis of ZnVAr under air atmosphere (Figure S5c) shows a weight loss at the beginning due to the loss of absorbed water and the combustion of carbon and weight gain at ca. 300-400 ^oC, indicative of vanadium in a lower oxidation state in the sample.[46] If we compare ZnVAr with ZnVair, the Zn concentration is about the same, but some V has disappeared during the calcination process to make ZnVAr, leading to a higher Zn/V ratio (1.613). The experimental residual mass by TGA is 96.25%, close to the residual mass calculated from the ICP data of 98.34%. For ZnVC the concentration of both Zn and V is lower (34.87% and 16.02%) due to the presence of a significant amount of carbon, and the Zn/V atom ratio is even higher at 1.695. The weight loss due to absorbed water in the materials is 3.50% (Figure S5d). The loss of weight during thermal decomposition is about 25.56%, a combined effect of combustion of the carbon to CO_2 and the oxidation of vanadium. The residual mass is 71.04%, very close to the value calculated from ICP data of 72.02%.

Therefore, the ratio of Zn to V increases from 1.54 to 1.695 after the carbon coating process, indicating ca. 9% V loss, which might be caused by the evaporation of V_2O_5(g) at high temperature during the calcination step. The ratio of Zn to V corresponds to a ratio of ZnO to ZnV_2O_4 of 2.39 in porous core-

shell ZnVC. There is about 25% carbon in ZnVC from starch in the precursor synthesis and from dopamine in the coating process. Assuming that all vanadium is V^{3+} in the product, the stoichiometry of the calcination of ZnVC corresponds to:

$$Zn_3(OH)_2(V_2O_7)(H_2O)_2 + 1.78\ C \rightarrow 2.11\ ZnO + 0.89\ ZnV_2O_4 + 0.11\ V_2O_5(g) + 3\ H_2O(g) + 1.78\ CO(g) \quad (3)$$

Table 2 *Zn and V mass concentration determined by ICP and residual mass after heating in air determined by TGA*

Samples	*ZnVS*	*ZnVair*	*ZnVAr*	*ZnVC*
Zn concentration (w%)	*34.26*	*47.13*	*46.67*	*34.87*
V concentration (w%)	*17.33*	*23.72*	*22.54*	*16.02*
Zn/V atom ratio	*1.540*	*1.547*	*1.613*	*1.695*
Experimental TGA residual mass	*68.80%*	-	*96.25%*	*71.04%*
Residual mass calculated from ICP data	*73.58%*	*101.02%*	*98.34%*	*72.02%*

3.4 Determination of porosity

The porosity and surface area are crucial for LIB electrodes. The nitrogen adsorption-desorption isotherms and the corresponding pore size distribution of the ZnVair, ZnVAr and ZnVC are measured to further investigate the porosity of the products. As shown in Figure 4a, The Brunauer–Emmett–Teller (BET) surface area of the ZnVair nanoparticles is ca. 21 $m^2\ g^{-1}$. The corresponding Barrett-Joyner-Halenda pore size distribution is displayed in Figure 4d, with an average pore size of ca. 40 nm and pore volume of 0.12 $cm^3\ g^{-1}$. The product ZnVAr (Figure 4b and e) possesses a very high specific surface area of 117 $m^2\ g^{-1}$, with many mesopores of up to 50 nm and a high pore volume of 0.29 $cm^3\ g^{-1}$. Interestingly, the specific surface area of ZnVC has the same high value of 115 $m^2\ g^{-1}$ and pore volume of 0.27 $cm^3\ g^{-1}$, but contains more mesopores (Figure 4c and 4f). Literature values of the BET surface area of vanadium-based metal oxides applied as lithium-ion batteries are collected in Table S1. For example, Xue et al.[60] synthesized hierarchical lychee-like $Zn_3V_3O_8$@C/rGO nanospheres with a surface area of 20 $m^2\ g^{-1}$. Balaji et al.[61] fabricated porous $Zn_3V_2O_8$ sheets with a surface area of 22 $m^2\ g^{-1}$, with improved diffusion kinetics due to a shorter diffusion pathway. Compared to this, the porous ZnVC

material presented here has a significantly higher specific surface area. We suggest that the high specific surface area and the high porosity provide more active sites and facilitate Li-ion diffusion. With the help of the carbon layer, the anode materials can more efficiently accommodate the volume variation during the charge and discharge process.

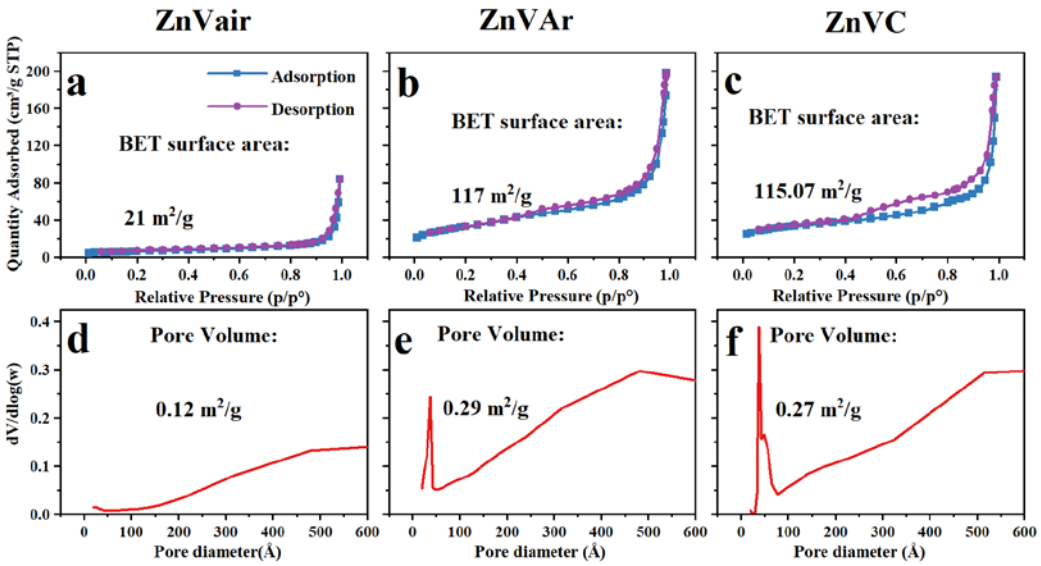

Figure 4. N_2 adsorption-desorption isotherms of the products and their corresponding pore size distributions: ZnVair (a) and (d); ZnVAr (b) and (e); ZnVC (c) and (f).

3.5 Electrochemical performance

The electrochemical performance as LIB anode materials is investigated in various electrochemical tests by using a CR2032 type coin half-cell assembled with Li metal cathode. The typical cyclic voltammogram (CV) curves during the second scan are recorded in a potential range of 0.02-3.0 V at a scan rate of 0.1 mV s^{-1} (Figure 5). For pure $Zn_3V_2O_8$ nanoparticles, the obvious reduction peaks at ca. 0.5 and 0.8 V are attributed to the reduction of V^{5+} to V^{4+} and V^{3+} along with the reduction of Zn^{2+} to metallic Zn.[62] The irreversible side reaction of solid electrolyte (SEI) interphase formation with metallic Zn further alloyed to form Li-Zn occurs at ca. 0.02 V.[63] For the oxidation process, there are three peaks at ca. 0.3 and 1.4 V, corresponding to the de-lithiation of Li-Zn alloys and the oxidation of Zn^0 to Zn^{2+}, respectively.[59, 64] The same peaks are observed for ZnVAr and the capacity is mainly due to faradic capacitance on the material.[65] For ZnVC, the same peaks as for ZnVAr are observed and there is one clearer oxidation peak at 2.5 V. The extra peak is assigned to the extraction of Li^+ from Li_xVO_2. The

porous core-shell ZnVC exhibits both double layer capacity from carbon and faradaic capacity from redox reactions.

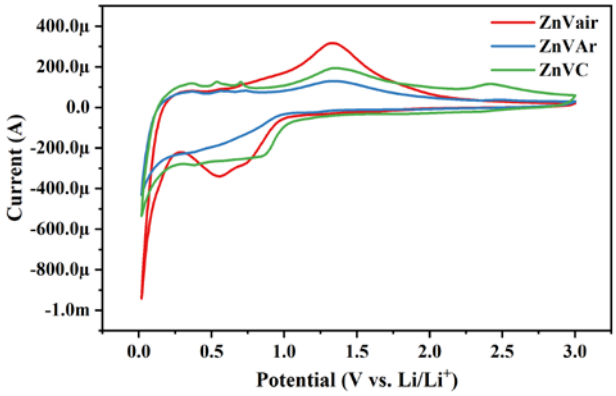

Figure 5. CV curves of ZnVair, ZnVAr and ZnVC at 0.1 mV s^{-1}.

The charge/discharge profiles of the ZnVair, ZnVAr and ZnVC anode materials for the initial two cycles and the 35th cycle at a current density of 100 mA g^{-1} are given in Figure 6a-c. The charge and discharge curves show plateaus at the same potential after the initial cycle. The difference in the initial discharge curve is due to the different chemical compositions in the as-synthesized materials. In the first discharge curve for ZnVair, a voltage decrease at 1.5V indicates the decomposition of the active ZnVair into ZnO, along with the formation of $Li_xV_2O_5$; the plateau at 0.8 V can be assigned to the reduction of ZnO into Zn^0; The two plateaus at 0.3 and 0.1 V are related to the irreversible reaction of the SEI layer by the formation of Li_2O and Li-Zn alloy.[66] The first charge curve shows a slope from 1.0 to 1.5 V, corresponding to the broad peak in the CV curve (Figure 5). The crystal phase in ZnVair is $Zn_3V_2O_8$ with V^{5+}, which potentially can transfer 15 electrons from 1 mol of $Zn_3V_2O_8$, resulting in a high initial discharge capacity of 1320 mAh g^{-1}. The coulombic efficiency is only 65%, due to side reactions of the SEI layer formation at the surfaces of the nanoparticles. In the following cycles, the plateaus are not obvious, indicating severe polarization, and the capacity decreases seriously to 267 mAh g^{-1} at the 35th cycle. In the initial discharge curve of ZnVAr a decomposition process takes place at 1.5 V, reduction of Zn at 1.0V, and the formation of Li-Zn alloy at 0.1 V. Since the main crystal phases in ZnVAr are ZnV_2O_4 and ZnO, vanadium is in oxidation state V^{3+}, leading to fewer electrons to transfer compared to ZnVair. Thus the initial discharge capacity is significantly lower (837 mAh g^{-1}).The initial coulombic efficiency is ca. 66% and the reversible capacity after 35 cycles is more stable at a value of 306 mAh g^{-1}. The same crystal phases are present in ZnVAr and ZnVC, and the initial discharge capacity of ZnVC

is 860 mAh g^{-1}, close to the value for ZnVAr. The initial discharge curves follow the same trend. The reversible capacity is very stable and the same value of 620 mAh g^{-1} is found after both 2 and after 35 cycles of charging and discharging at 100 mA g^{-1}. The plateaus during charge and discharge of the ZnVC are obvious even after 35 cycles, due to the stability of the material.[67] In order to investigate the stability of the anode materials further, the cycling performance is tested at a high current density of 500 mA g^{-1} after 35 or 50 cycles (Figure 6d-6f). The capacity of ZnVair (Figure 6d) decreases severely from 1320 to 267 mAh g^{-1} at a current density of 100 mA g^{-1}. At a current density of 500 mA g^{-1}, the capacity is even lower, 70 mAh g^{-1}. After 200 cycles, the capacity gradually climbs to 161 mAh g^{-1}. For ZnVAr (Figure 6e) the value at cycle 35 is 299 mAh g^{-1}. At a higher current density, the capacity is stable at 225 mAh g^{-1} even after 200 cycles. Very interestingly, ZnVC exhibits a super stable capacity of 620 mAh g^{-1} in the initial 50 cycles at a current density of 100 mA g^{-1}, (Figure 6f) and a reversible capacity of 404 mAh g^{-1} in the following 200 cycles at a high current density of 500 mAh g^{-1}. Though ZnVair ($Zn_3V_2O_8$) and ZnVAr (ZnV_2O_4/ZnO) are different initially and ZnVair has a much higher theoretical capacity than ZnVAr, the ZnVAr still delivers higher capacity than ZnVair, indicating that the porous structure contributes to a better performance. ZnVAr and ZnVC have the same metal oxide composition and morphology, but ZnVC shows a much more stable electrochemical performance, which is suggested to be the effect of nitrogen-doped carbon coating. According to the CV curves and charge discharge curves, the reactions during charge and discharge can be summarized as follows:[39, 68] Equation (4) and (5) describe the initial discharge, (6)-(8) are the reversible charge (forward arrow) and discharge (back arrow) reactions. Compounds written in bold are observed by PXRD:

$$\mathbf{ZnV_2O_4} + (2x + y)\,\mathrm{Li^+} + (2x + y)\,\mathrm{e^-} \rightarrow 2\,\mathbf{Li_xVO_2} + \mathbf{Li_yZn} \quad (4)$$

$$\mathbf{ZnO} + (y + 2)\,\mathrm{Li^+} + (y + 2)\,\mathrm{e^-} \rightarrow \mathbf{Li_yZn} + \mathrm{Li_2O} \quad (5)$$

$$\mathbf{Li_xVO_2} \rightleftharpoons \mathbf{LiVO_2} + (x - 1)\,\mathrm{Li^+} + (x - 1)\,\mathrm{e^-} \quad (6)$$

$$\mathbf{Li_yZn} \rightleftharpoons \mathrm{Zn} + y\,\mathrm{Li^+} + y\,\mathrm{e^-} \quad (7)$$

$$\mathrm{Zn} + \mathrm{Li_2O} \rightleftharpoons \mathbf{ZnO} + 2\,\mathrm{Li^+} + 2\,\mathrm{e^-} \quad (8)$$

$1 \leq x \leq 2,\ y \leq 1$

As written above, the ratio of ZnO to ZnV_2O_4 in porous core-shell ZnVC is about 2.39 with a weight percentage of about 25% carbon, indicating 53% ZnO and 22% ZnV_2O_4. The maximum number of electrons that could be transferred for ZnV_2O_4 would be 5, and for ZnO, there are 2 electrons for the reduction process and 1 electron for the alloying process. Thus the theoretical specific capacity could be calculated by the formula:[69]

$$C_{th} = \frac{nF}{3.6\, M_w} \tag{8}$$

where *n* is the number of the electrons that the material could transfer, *F* is Faradays constant (96485 C mol^{-1}) and M_w is the molar mass (g mol^{-1}). Using this, the maximum theoretical capacity of ZnVC is calculated to be 651 mAh g^{-1} disregarding any contribution from the carbon layer to the capacity. The initial discharge capacity of the ZnVC is 860 mAh g^{-1}, and the coulombic efficiency is 72%, due to the irreversible capacity formation of the SEI film and incomplete restoration to original active materials.[70] After the second cycle of the ZnVC, the value is stable at 620 mAh g^{-1} during the following 49 cycles at a current density of 100 mA g^{-1}, very close to the theoretical capacity of this material, indicating the full utilization of the material. The electrochemical performance in terms of capacity and cycling performance of the ZnV_2O_4 is better than most of the reported ZnV_2O_4 materials. For example, ZnV_2O_4/ordered mesoporous carbon (CMK) nanocomposite obtained by a direct precipitation and calcination process exhibited 575 mAh g^{-1} at a current density of 100 mA g^{-1} after 200 cycles.[71] The porous ZnVC also outperforms LTO and other metal oxides, as shown in Table S2, such as TiO_2 nanoparticles, [72] $HfNb_{24}O_{62}$,[73] $Nb_{12}O_{29}$.[74]

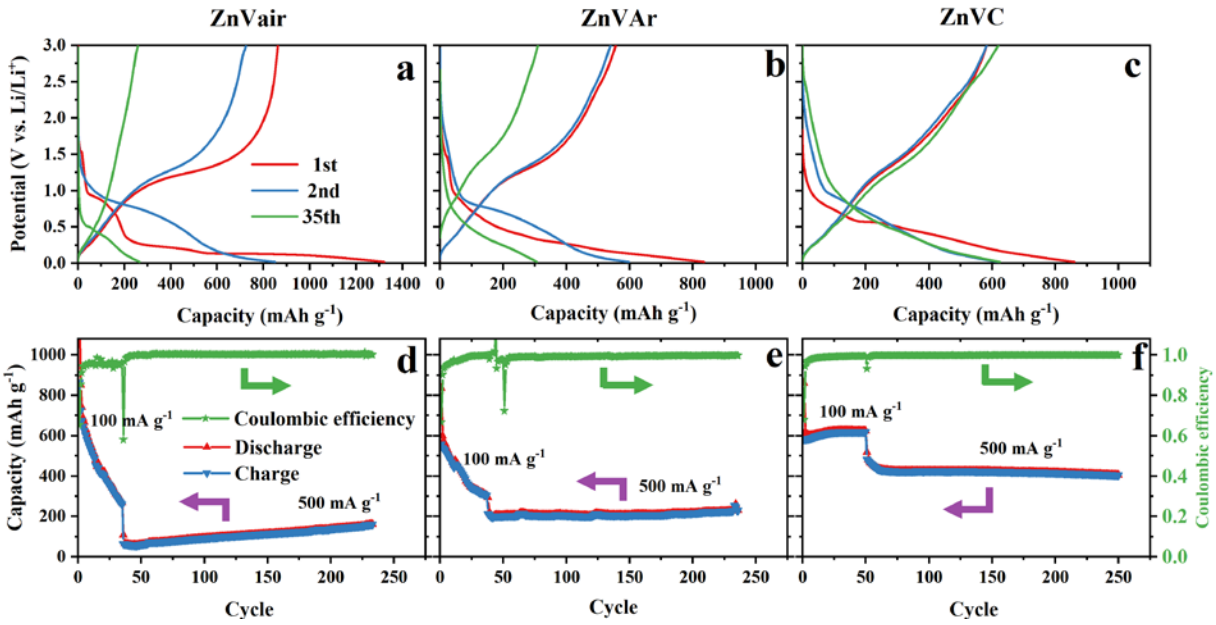

Figure 6. Galvanostatic discharge/charge curves of the 1st 2nd and 35th cycles of ZnVair (a), ZnVAr (b) and ZnVC (c). Charge-discharge cycling performances and coulombic efficiency of battery anodes based on ZnVair (d), ZnVAr (e) and ZnVC (f).

In battery applications, it is generally observed that materials consisting of particles perform worse than porous structures, due to particles aggregating during the charge and discharge process. Therefore, the morphology of the materials is investigated by SEM and TEM after cycling. The ZnVair nanoparticles (Figure 7a and d) have aggregated to form large particles, but some of the porous ZnVAr flakes and most of the porous ZnVC maintain the morphology. Porous ZnVAr (Figure 7b and e) breaks into nanoparticles. Interestingly, ZnVC (Figure 7c and f) still retains the flower morphology with an unchanged size of ca. 500 nm. Moreover, the core-shell structure is easily observed (Figure S6a). Figure S6b shows the linear scan EDS element analysis by HAADF-STEM. Zinc and vanadium are present in the centre and carbon at the edges, indicating that the core-shell structure is stable during the cycling process. XRD is also applied to test the crystalline phases of the materials after extensive cycling. The results after the final discharge process (0.02 V) are shown in Figure S7a. For ZnVair the peaks in the XRD are very week after cycling compared to before cycling (Figure 1g). The XRD peaks observed for ZnVAr and ZnVC after extended cycling are also weak, but there is less change from before the testing of the materials. The peaks can be assigned to $Zn_{1.98}Li_{0.02}$ (ICOD:96-153-7986) alloy as well as the spinel phase ZnV_2O_4 (ICOD:01-089-7413), which was present also before testing. The ZnV_2O_4 phase is more apparent in ZnVAr than in ZnVC and the fact that it is still present after discharge could indicate

a less sufficient utilization of the material. In the fully charged state (3.0 V), the vanadium is primarily in a $LiVO_2$ phase (COD: 96-152-9720), and the zinc is in a ZnO phase (ICOD: 00-001-1136), as shown in Figure S7b. Due to the irreversible reactions in ZnVair, the ZnO phase is hardly observed, comparing to ZnVAr and ZnVC.

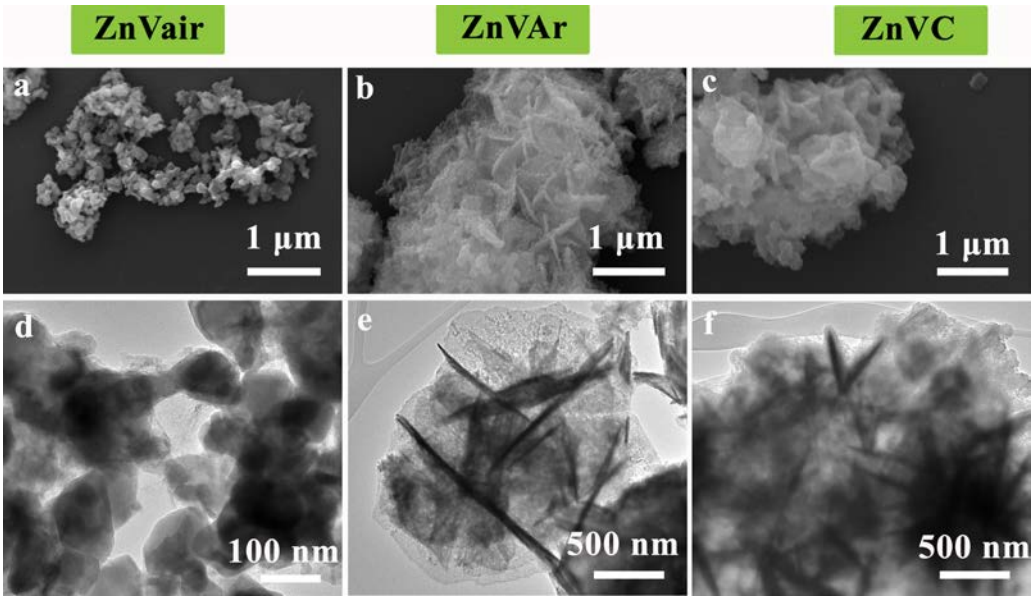

Figure 7. SEM and TEM images of ZnVair (a, d), ZnVAr (b, e) and ZnVC (c, f) after long-term cycling.

The samples are also tested by galvanostatic discharge/charge at different current densities. As shown in Figure S8, the reversible capacity of the ZnVair nanoparticles exhibits discharge capacities of 400, 243, 147 and 73 mAh g^{-1} at current densities of 100, 200, 400 and 800 mA g^{-1}, respectively. In contrast, the porous ZnVAr and ZnVC exhibit much better rate capacities. For ZnVAr the reversible capacities are 594, 463, 343 and 221 mAh g^{-1} and for ZnVC they are 620, 477, 368, and 259 mAh g^{-1} at these current densities, respectively. The rate performance is also a significant criterion for electrochemical performance. The ZnVAr and ZnVC both exhibit great capacity, benefiting from the porous structure that facilitates the diffusion of Li ions during the fast charge and discharge process. We suggest that the relatively high reversible capacity of the ZnVC material is due to the improved electrical conductivity from the added carbon layer.

The electrochemical properties of all materials were investigated by EIS which is a common method to reveal the electron transfer resistance at the open-circuit voltage and the negative permittivity.[75] In Figure S9a, the plots reveal semicircles in the high-frequency region and straight line in the low-

frequency region. The value of the intercept with the x-axis is the bulk resistance of the cell, reflecting the conductivity of the electrolyte and the separator resistance Rs in the range 10 to 13 Ω. The semicircle in the plot is related to the Faradaic charge transfer resistance and its relative double-layer capacitance, and the linear part is related to a combination of the diffusional effects of Li-ion on the interface between the active material and electrolyte. According to the diameter of the semicircles, the charge transfer impedance (Rct) can be obtained. A low Rct generally corresponds to fast kinetics of the Faradaic reaction.[76-77] ZnVC (32 Ω) has a lower Rct than those of ZnVAr (139 Ω) and ZnVair (118 Ω) anodes, indicating that the conductivity of the ZnVC anode is superior. The Li^+ diffusion coefficient can be calculated from the following formula:[78]

$$Z' = \mathrm{Rs} + \mathrm{Rct} + A_w w^{-\frac{1}{2}} \quad (1)$$

$$D_{Li^+} = [\frac{V_m}{FAA_w}\left(-\frac{dE}{dx}\right)]^2 \quad (2)$$

Here *Z*' is the real impedance collected during the experiment; A_w is the Warburg coefficient, which is the diffusion coefficient of ions in solution; *w* is angular frequency; V_m is the molar volume of the samples; *dE/dx* is the slope of the open-circuit voltage proportional to the concentration of Li^+; *A* is the surface area of the electrode; *F* is the Faraday constant.[78] As shown in Figure S9 b, the Warburg coefficient A_w is equal to the slope of the *Z*' vs. $w^{-1/2}$ line at low frequency and can be estimated according to Eq. 1. The EIS parameters are collected in Table 4. Eq. 2 indicates that D_{Li+} is mainly determined by $(1/A_w)^2$ and that a small value of A_w implies a high Li^+ diffusion coefficient.[79] As shown in Table 4, the fresh ZnVair nanoparticles have the lowest A_w (52.2 Ω $s^{-1/2}$) compared to fresh ZnVAr (414.5 Ω $s^{-1/2}$) and ZnVC (149.3 Ω $s^{-1/2}$). It is anticipated that ion conductivity in materials consisting of nanoparticles would be found to be higher than for the porous structure-material ZnVC. The same phenomenon has been observed in our previous work.[80] After the cycling test, ZnVC (52 Ω) has the lowest electron transfer resistance Rct compared to ZnVair (653 Ω) and ZnVAr (305 Ω). In addition, the porous ZnVC also has the lowest Warburg coefficient, about 61.9 Ω $s^{-1/2}$. ZnVC shows better ion conductivity than that of ZnVAr and ZnVair nanoparticles because the porous structure buffers the volume change during the cycling process, and the carbon layer helps to maintain the structural integrity.

However, the measured impedance of the cell has contributions from all components, and if the cell is activated, the impedance spectra will become more complicated. It is difficult to single out the contribution of the working electrode because the impedance spectrum in a two-electrode experiment is a combination of the contributions from the positive and negative electrode. Therefore, a three-electrode system (EL-CELL GmbH, Germany) is applied to investigate the contribution of the active material in the second cycle (Figure 8a). The counter and reference electrodes are both Li metal. In the three-electrode experiment the individual impedances of the electrodes versus the reference electrode is determined giving impedance contributions at the same time: counter and reference, reference and working electrode, and counter and the working electrode (Figure 8d). To understand the effects on the impedance of the Li-ion insertion and extraction in the working electrode, the cell is charged and discharged to a certain potential and the EIS experiment is performed when the reactions reach equilibrium. Interestingly, the charge transfer impedance Rct (Figure 8b) gradually increases with more Li-ion extraction from the working electrode. The oblique linear Warburg part is fitted in Figure S9c, and the Warburg coefficient (A_w) is equal to the slope to the Z' vs. $w^{-1/2}$ line at low frequency. The response is reversible during the discharge process (Figure 8e and f), indicating the stability of the porous core-shell ZnVC.

Table 4 *EIS parameters of the anode electrode before and after cycling test.*

	Fresh electrode			*Electrode after cycling*		
	Rs (Ω)	*Rct (Ω)*	*Aw (Ω $s^{-1/2}$)*	*Rs (Ω)*	*Rct (Ω)*	*Aw (Ω $s^{-1/2}$)*
ZnVair	*10*	*118*	*52.2*	*20*	*653*	*72.6*
ZnVAr	*13*	*139*	*414.5*	*52*	*305*	*1078.2*
ZnVC	*13*	*32*	*149.3*	*28*	*52*	*61.9*

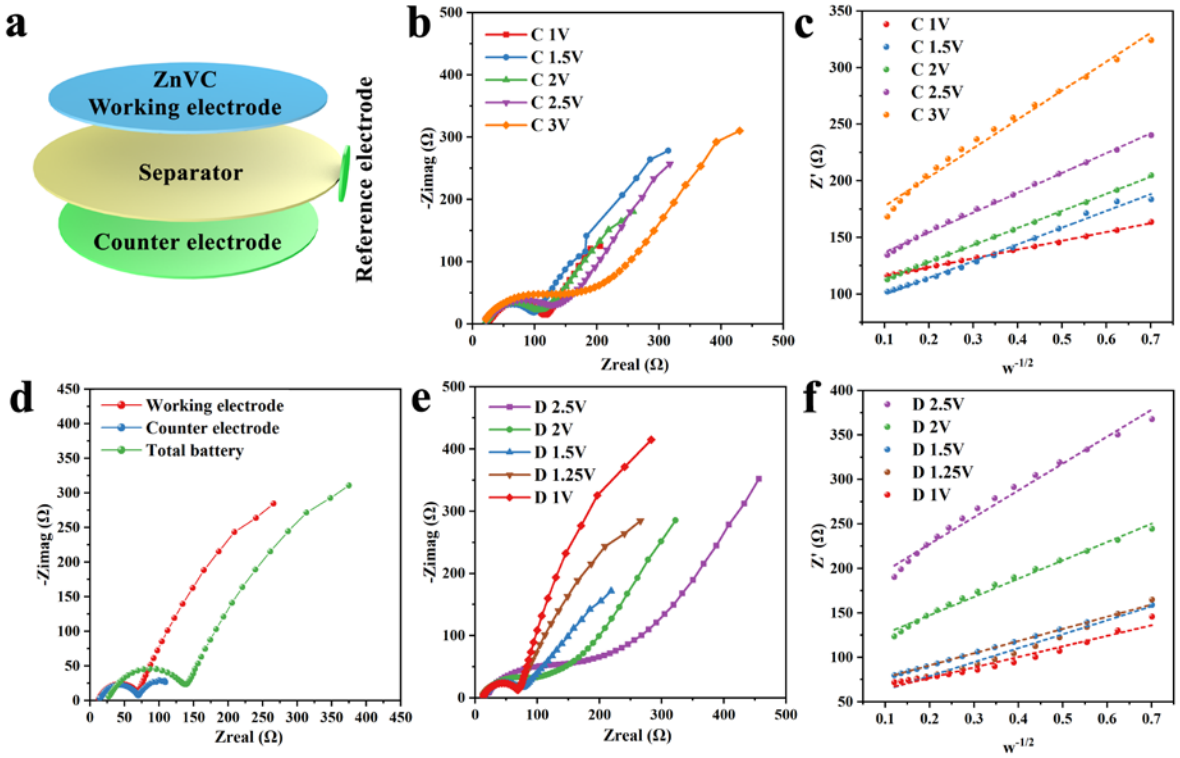

Figure 8. Visualization of the setup of the three-electrode system with ZnVC coated on the working electrode (a); impedance spectra of the working electrode during charging (b) and the corresponding linear fitting of the square root of Warburg impedance with real part Z' obtained for Nyquist plot (c); and the full cell impedance spectra (d); the impedance spectra of the working electrode during discharge process (e) and the corresponding linear fitting (f).

4. Conclusions

In conclusion, porous ZnV_2O_4/ZnO@N-doped carbon with a high specific surface area of 115 m^2 g^{-1} has been obtained from flower-like $Zn_3(OH)_2(V_2O_7)(H_2O)_2$ coated with polymer dopamine by calcination in Ar. During the calcination process, the ratio of Zn and V is maintained at 1.695 after some loss of vanadium, and the vanadium is reduced from V^{5+} to V^{3+} due to the presence of carbon. When used as an anode electrode of LIBs, ZnV_2O_4/ZnO@N-doped carbon exhibits a very stable specific capacity of 620 mAh g^{-1} at a current density of 100 mA g^{-1}. This excellent performance is

caused by the high electronic conductivity and ionic conductivity. In addition, the charge transfer impedance of the ZnV_2O_4/ZnO@N-doped carbon increases at high potential, and the Li-ion diffusion coefficient decreases.

Associated content

Supporting Information

Additional information and figures including the SEM image of ZnVS and TEM images of ZnVair, and ZnVAr. Raman spectra of core-shell ZnVC; ICP standard curves. V2p XPS spectra; TGA curves of ZnVS, ZnVAr, and ZnVC. TEM image and EDS element analysis of the ZnVC after 250 cycles; Rate capability curves of the ZnVair, ZnVAr, and ZnVC; Nyquist plots of porous ZnVair, ZnVAr, and ZnVC and the corresponding linear fitting of the square root of Warburg impedance with real part Z'.

Notes

There are no conflicts to declare.

Acknowledgements

The authors gratefully acknowledge the financial support from the China Scholarship Council for a Ph.D. scholarship (No. 201706220078) to H. C. and a H. C. Ørsted COFUND Scholarship to X. X.

Data availability

Raw data from all measurements are available from the authors.

References

[1] K. Wang, Y. Chen, R. Tian, H. Li, Y. Zhou, H. Duan, H. Liu, Porous Co–C Core–Shell Nanocomposites Derived from Co-MOF-74 with Enhanced Electromagnetic Wave Absorption Performance, ACS Appl. Mater. Interfaces, 10 (2018) 11333-11342.

[2] Z. Cui, H. Yin, Q. Nie, Controllable preparation of hierarchically core–shell structure NiO/C microspheres for non-enzymatic glucose sensor, J. Alloys Compd., 632 (2015) 402-407.

[3] E. Lim, C. Jo, H. Kim, M.-H. Kim, Y. Mun, J. Chun, Y. Ye, J. Hwang, K.-S. Ha, K. C. Roh, K. Kang, S. Yoon, J. Lee, Facile Synthesis of Nb_2O_5@Carbon Core–Shell Nanocrystals with Controlled Crystalline Structure for High-Power Anodes in Hybrid Supercapacitors, ACS Nano, 9 (2015) 7497-7505.

[4] B. Sun, Z. Chen, H.-S. Kim, H. Ahn, G. Wang, MnO/C core–shell nanorods as high capacity anode materials for lithium-ion batteries, J. Power Sources, 196 (2011) 3346-3349.

[5] S. Wang, Y. Zhu, X. Xu, J. Sunarso, Z. Shao, Adsorption-based synthesis of Co_3O_4/C composite anode for high performance lithium-ion batteries, Energy, 125 (2017) 569-575.

[6] X. H. Rui, C. Li, C. H. Chen, Synthesis and characterization of carbon-coated $Li_3V_2(PO_4)_3$ cathode materials with different carbon sources, Electrochim. Acta, 54 (2009) 3374-3380.

[7] Y. Huang, H. Ren, S. Yin, Y. Wang, Z. Peng, Y. Zhou, Synthesis of $LiFePO_4$/C composite with high-rate performance by starch sol assisted rheological phase method, J. Power Sources, 195 (2010) 610-613.

[8] H. Li, L. Shen, K. Yin, J. Ji, J. Wang, X. Wang, X. Zhang, Facile synthesis of N-doped carbon-coated $Li_4Ti_5O_{12}$ microspheres using polydopamine as a carbon source for high rate lithium ion batteries, J. Mater. Chem. A, 1 (2013) 7270-7276.

[9] G. Zou, H. Hou, G. Zhao, P. Ge, D. Yin, X. Ji, N-rich carbon coated $CoSnO_3$ derived from in situ construction of a Co–MOF with enhanced sodium storage performance, J. Mater. Chem. A, 6 (2018) 4839-4847.

[10] G. Lu, S. Qiu, J. Liu, X. Wang, C. He, Y.-J. Bai, Enhanced Electrochemical Performance of Zn-Doped Fe_3O_4 with Carbon Coating, Electrochim. Acta, 117 (2014) 230-238.

[11] G. Lu, S. Qiu, H. Lv, Y. Fu, J. Liu, X. Li, Y.-J. Bai, Li-Ion Storage Performance of MnO Nanoparticles Coated with Nitrogen-Doped Carbon Derived from Different Carbon Sources, Electrochim. Acta, 146 (2014) 249-256.

[12] Z. Ding, L. Zhao, L. Suo, Y. Jiao, S. Meng, Y.-S. Hu, Z. Wang, L. Chen, Towards understanding the effects of carbon and nitrogen-doped carbon coating on the electrochemical performance of $Li_4Ti_5O_{12}$ in lithium ion batteries: a combined experimental and theoretical study, Phys. Chem. Chem. Phys., 13 (2011) 15127-15133.

[13] M. Idrees, S. Batool, J. Kong, Q. Zhuang, H. Liu, Q. Shao, N. Lu, Y. Feng, E. K. Wujcik, Q. Gao, T. Ding, R. Wei, Z. Guo, Polyborosilazane derived ceramics - Nitrogen sulfur dual doped graphene nanocomposite anode for enhanced lithium ion batteries, Electrochim. Acta, 296 (2019) 925-937.

[14] C. Shi, H. Qi, R. Ma, Z. Sun, L. Xiao, G. Wei, Z. Huang, S. Liu, J. Li, M. Dong, J. Fan, Z. Guo, N,S-self-doped carbon quantum dots from fungus fibers for sensing tetracyclines and for bioimaging cancer cells, Mater. Sci. Eng. C, 105 (2019) 110132.

[15] J. Tan, D. Li, Y. Liu, P. Zhang, Z. Qu, Y. Yan, H. Hu, H. Cheng, J. Zhang, M. Dong, C. Wang, J. Fan, Z. Li, Z. Guo, M. Liu, A self-supported 3D aerogel network lithium–sulfur battery cathode: sulfur spheres wrapped with phosphorus doped graphene and bridged with carbon nanofibers, J. Mater. Chem. A, 8 (2020) 7980-7990.

[16] X. Zhang, K. S. Ziemer, B. L. Weeks, Combustion synthesis of N-doped three-dimensional graphene networks using graphene oxide–nitrocellulose composites, Adv. Comp. Hybrid Mater., 2 (2019) 492-500.

[17] J. Huang, Y. Li, Y. Cao, F. Peng, Y. Cao, Q. Shao, H. Liu, Z. Guo, Hexavalent chromium removal over magnetic carbon nanoadsorbents: synergistic effect of fluorine and nitrogen co-doping, J. Mater. Chem. A, 6 (2018) 13062-13074.

[18] M. Idrees, L. Liu, S. Batool, H. Luo, J. Liang, B. Xu, S. Wang, J. Kong, Cobalt-Doping Enhancing Electrochemical Performance of Silicon/Carbon Nanocomposite as Highly Efficient Anode Materials in Lithium-Ion Batteries, Eng. Sci., 6 (2019) 64-76.

[19] H. Chen, Q. Luo, T. Liu, M. Tai, J. Lin, V. Murugadoss, H. Lin, J. Wang, Z. Guo, N. Wang, Boosting Multiple Interfaces by Co-Doped Graphene Quantum Dots for High Efficiency and Durability Perovskite Solar Cells, ACS Appl. Mater. Interfaces, 12 (2020) 13941-13949.

[20] B. Song, Q. Wang, L. Wang, J. Lin, X. Wei, V. Murugadoss, S. Wu, Z. Guo, T. Ding, S. Wei, Carbon nitride nanoplatelet photocatalysts heterostructured with B-doped carbon nanodots for enhanced photodegradation of organic pollutants, J. Colloid Interface Sci., 559 (2020) 124-133.

[21] H. Yu, L. Yang, D. Cheng, D. Cao, Zeolitic-imidazolate Framework (ZIF)@ZnCo-ZIF Core-shell Template Derived Co, N-doped Carbon Catalysts for Oxygen Reduction Reaction, Eng. Sci., 3 (2018) 54-61.

[22] X. Wu, W. Li, P. Wu, C. Ma, Y. Liu, M. Xu, S. Liu, Long-Lived Room-Temperature Phosphorescent Nitrogen-Doped CQDs/PVA Composites: Fabrication, Characterization and Application, Eng. Sci., 4 (2018) 111-118.

[23] H. Dong, Y. Li, H. Chai, Y. Cao, X. Chen, Hydrothermal Synthesis of $CuCo_2S_4$ Nano-structure and N-Doped Graphene for High-Performance Aqueous Asymmetric Supercapacitors, ES Energy Envir., 4 (2019) 19-26.

[24] C. Zhang, Y. Xie, H. Deng, C. Zhang, J.-W. Su, J. Lin, Nitrogen Doped Coal with High Electrocatalytic Activity for Oxygen Reduction Reaction, Eng. Sci., 8 (2019) 39-45.

[25] H. Zhao, J. Li, H. Wu, T. Dong, Y. Zhang, H. Liu, Dopamine Self‐Polymerization Enables an N‐Doped Carbon Coating of Exfoliated MoS_2 Nanoflakes for Anodes of Lithium‐Ion Batteries, ChemElectroChem, 5 (2018) 383-390.

[26] Y. Wang, Q. Qu, G. Li, T. Gao, F. Qian, J. Shao, W. Liu, Q. Shi, H. Zheng, 3D Interconnected and Multiwalled Carbon@MoS_2@Carbon Hollow Nanocables as Outstanding Anodes for Na-Ion Batteries, Small, 12 (2016) 6033-6041.

[27] Y. Lv, L. Zhu, H. Xu, L. Yang, Z. Liu, D. Cheng, X. Cao, J. Yun, D. Cao, Core/shell Template-derived Co, N-doped Carbon Bifunctional Electrocatalysts for Rechargeable Zn-air Battery, Eng. Sci., 7 (2019) 26-37.

[28] Y. Zhai, J. Wang, Q. Gao, Y. Fan, C. Hou, Y. Hou, H. Liu, Q. Shao, S. Wu, L. Zhao, T. Ding, F. Dang, Z. Guo, Highly efficient cobalt nanoparticles anchored porous N-doped carbon nanosheets electrocatalysts for Li-O_2 batteries, J. Catal., 377 (2019) 534-542.

[29] X. Wang, X. Zeng, D. Cao, Biomass-derived Nitrogen-doped Porous Carbons (NPC) and NPC/ Polyaniline Composites as High Performance Supercapacitor Materials, Eng. Sci., 1 (2018) 55-63.

[30] J. Chen, X. Wang, Y. Huang, S. Lv, X. Cao, J. Yun, D. Cao, Adsorption Removal of Pollutant Dyes in Wastewater by Nitrogen-doped Porous Carbons Derived from Natural Leaves, Eng. Sci., 5 (2018) 30-38.

[31] X. Xue, H. Yan, Y. Fu, Preparation of pure and metal-doped $Li_4Ti_5O_{12}$ composites and their lithium-storage performances for lithium-ion batteries, Solid State Ionics, 335 (2019) 1-6.

[32] N. Zhu, W. Liu, M. Xue, Z. Xie, D. Zhao, M. Zhang, J. Chen, T. Cao, Graphene as a conductive additive to enhance the high-rate capabilities of electrospun $Li_4Ti_5O_{12}$ for lithium-ion batteries, Electrochim. Acta, 55 (2010) 5813-5818.

[33] H. Iuchi, T. Horikawa, K.-I. Sotowa, Synthesis and electrochemical performance of a nanocrystalline $Li_4Ti_5O_{12}$/C composite for lithium-ion batteries prepared using resorcinol–formaldehyde resins, Electrochim. Acta, 295 (2019) 540-549.

[34] B. Zhao, R. Ran, M. Liu, Z. Shao, A comprehensive review of $Li_4Ti_5O_{12}$-based electrodes for lithium-ion batteries: The latest advancements and future perspectives, Mater. Sci. .Eng. R: Reports, 98 (2015) 1-71.

[35] L. Sun, J. Wang, K. Jiang, S. Fan, Mesoporous $Li_4Ti_5O_{12}$ nanoclusters as high performance negative electrodes for lithium ion batteries, J. Power Sources, 248 (2014) 265-272.

[36] M. He, M. Walter, K. V. Kravchyk, R. Erni, R. Widmer, M. V. Kovalenko, Monodisperse SnSb nanocrystals for Li-ion and Na-ion battery anodes: synergy and dissonance between Sn and Sb, Nanoscale, 7 (2015) 455-459.

[37] D. Bresser, S. Passerini, B. Scrosati, Leveraging valuable synergies by combining alloying and conversion for lithium-ion anodes, Energ. Environ. Sci., 9 (2016) 3348-3367.

[38] Y. Lu, L. Yu, X. W. Lou, Nanostructured Conversion-type Anode Materials for Advanced Lithium-Ion Batteries, Chem, 4 (2018) 972-996.

[39] Z. Yin, J. Qin, W. Wang, M. Cao, Rationally designed hollow precursor-derived $Zn_3V_2O_8$ nanocages as a high-performance anode material for lithium-ion batteries, Nano Energy, 31 (2017) 367-376.

[40] L. Luo, Y. Fei, K. Chen, D. Li, X. Wang, Q. Wang, Q. Wei, H. Qiao, Facile synthesis of one-dimensional zinc vanadate nanofibers for high lithium storage anode material, J. Alloys Compd., 649 (2015) 1019-1024.

[41] X. Wang, S. Qiu, G. Lu, C. He, J. Liu, L. Luan, W. Liu, Fabrication of porous MnO microspheres with carbon coating for lithium ion battery application, CrystEngComm, 16 (2014) 1802-1809.

[42] T. Zhu, J. S. Chen, X. W. Lou, Glucose-Assisted One-Pot Synthesis of FeOOH Nanorods and Their Transformation to Fe_3O_4@Carbon Nanorods for Application in Lithium Ion Batteries, J. Phys. Chem. C, 115 (2011) 9814-9820.

[43] K. Tao, P. Li, L. Kang, X. Li, Q. Zhou, L. Dong, W. Liang, Facile and low-cost combustion-synthesized amorphous mesoporous NiO/carbon as high mass-loading pseudocapacitor materials, J. Power Sources, 293 (2015) 23-32.

[44] X. Li, J. Fu, Z. Pan, J. Su, J. Xu, B. Gao, X. Peng, L. Wang, X. Zhang, P. K. Chu, Peapod-like V_2O_3 nanorods encapsulated into carbon as binder-free and flexible electrodes in lithium-ion batteries, J. Power Sources, 331 (2016) 58-66.

[45] J. M. Won, Y. N. Ko, J.-K. Lee, Y. C. Kang, Superior electrochemical properties of rutile VO_2-carbon composite microspheres as a promising anode material for lithium ion batteries, Electrochim. Acta, 156 (2015) 179-187.

[46] C. Bie, J. Pei, G. Chen, Q. Zhang, J. Sun, Y. Yu, D. Chen, Hierarchical $Zn_3V_3O_8$/C composite microspheres assembled from unique porous hollow nanoplates with superior lithium storage capability, J. Mater. Chem. A, 4 (2016) 17063-17072.

[47] H. Yan, Y. Luo, X. Xu, L. He, J. Tan, Z. Li, X. Hong, P. He, L. Mai, Facile and Scalable Synthesis of $Zn_3V_2O_7(OH)_2{\cdot}2H_2O$ Microflowers as a High-Performance Anode for Lithium-Ion Batteries, ACS Appl. Mater. Interfaces, 9 (2017) 27707-27714.

[48] Q. Wei, F. Zhang, J. Li, B. Li, C. Zhao, Oxidant-induced dopamine polymerization for multifunctional coatings, Polym. Chem., 1 (2010) 1430-1433.

[49] J.-W. Oh, J. Heo, T. H. Kim, An electrochemically modulated single-walled carbon nanotube network for the development of a transparent flexible sensor for dopamine, Sensors and Actuators B: Chemical, 267 (2018) 438-447.

[50] C. Srinivas, M. Sudharsan, G. R. K. Reddy, P. S. Kumar, A. J. Amali, D. Suresh, Co/Co-N@Nanoporous Carbon Derived from ZIF-67: A Highly Sensitive and Selective Electrochemical Dopamine Sensor, Electroanalysis, 30 (2018) 2475-2482.

[51] S. Wang, Y. Xing, C. Xiao, H. Xu, S. Zhang, A peapod-inspired MnO@C core-shell design for lithium ion batteries, J. Power Sources, 307 (2016) 11-16.

[52] N. Wu, C. Liu, D. Xu, J. Liu, W. Liu, Q. Shao, Z. Guo, Enhanced Electromagnetic Wave Absorption of Three-Dimensional Porous Fe_3O_4/C Composite Flowers, ACS Sustain. Chem. Eng., 6 (2018) 12471-12480.

[53] Y. Tian, Y. An, C. Wei, B. Xi, S. Xiong, J. Feng, Y. Qian, Flexible and Free-Standing $Ti_3C_2T_x$ MXene@Zn Paper for Dendrite-Free Aqueous Zinc Metal Batteries and Nonaqueous Lithium Metal Batteries, ACS Nano, 13 (2019) 11676-11685.

[54] D. Chao, C. Zhu, M. Song, P. Liang, X. Zhang, N. H. Tiep, H. Zhao, J. Wang, R. Wang, H. Zhang, H. J. Fan, A High-Rate and Stable Quasi-Solid-State Zinc-Ion Battery with Novel 2D Layered Zinc Orthovanadate Array, Adv. Mater., 30 (2018) 1803181.

[55] Y. Tian, Y. An, H. Wei, C. Wei, Y. Tao, Y. Li, B. Xi, S. Xiong, J. Feng, Y. Qian, Micron-Sized Nanoporous Vanadium Pentoxide Arrays for High-Performance Gel Zinc-Ion Batteries and Potassium Batteries, Chem. Mater., 32 (2020) 4054-4064.

[56] H. Wu, Z. Zhang, M. Qin, Q. Wang, Z. Cao, Y. Yu, B. Jia, X. Qu, Solution combustion synthesis of crystalline V_2O_3 and amorphous V_2O_3/C as anode for lithium-ion battery, J. Am. Ceram. Soc., 103 (2020) 2643-2652.

[57] G. Haberfehlner, A. Orthacker, M. Albu, J. Li, G. Kothleitner, Nanoscale voxel spectroscopy by simultaneous EELS and EDS tomography, Nanoscale, 6 (2014) 14563-14569.

[58] H.-T. Zhang, L. Zhang, D. Mukherjee, Y.-X. Zheng, R. C. Haislmaier, N. Alem, R. Engel-Herbert, Wafer-scale growth of VO_2 thin films using a combinatorial approach, Nat. Commun., 6 (2015) 8475.

[59] R. Nie, G. Fang, J. Zhou, J. Guo, Y. Tang, S. Liu, Y. Cai, P. Hao, S. Liang, Three-dimensional $Zn_3V_3O_8$/carbon fiber cloth composites as binder-free anode for lithium-ion batteries, Electrochim. Acta, 246 (2017) 97-105.

[60] H. Xue, Y. Fang, L. Zeng, X. He, F. Luo, R. Liu, J. Liu, Q. Chen, M. Wei, Q. Qian, Facile synthesis of hierarchical lychee-like $Zn_3V_3O_8$@C/rGO nanospheres as high-performance anodes for lithium ion batteries, J. Colloid Interface Sci., 533 (2019) 627-635.

[61] B. Sambandam, V. Soundharrajan, J. Song, S. Kim, J. Jo, D. T. Pham, S. Kim, V. Mathew, J. Kim, $Zn_3V_2O_8$ porous morphology derived through a facile and green approach as an excellent anode for high-energy lithium ion batteries, Chem. Eng. J., 328 (2017) 454-463.

[62] C. Bie, J. Pei, J. Wang, K. Hua, D. Chen, G. Chen, Graphite Nanoplates Firmly Anchored with Well-dispersed Porous $Zn_3V_2O_8$ Nanospheres: Rational Fabrication and Enhanced Lithium Storage Capability, Electrochim. Acta, 248 (2017) 140-149.

[63] Y. An, Y. Tian, C. Wei, H. Jiang, B. Xi, S. Xiong, J. Feng, Y. Qian, Scalable and Physical Synthesis of 2D Silicon from Bulk Layered Alloy for Lithium-Ion Batteries and Lithium Metal Batteries, ACS Nano, 13 (2019) 13690-13701.

[64] J. Zhou, B. Zhao, J. Bai, Z. Fang, K. Li, H. Ma, J. Dai, X. Zhu, Y. Sun, Three-dimensional porous Zn_2VO_4/ZnO/C thin film anode materials for high-performance Li-ion batteries, Scr. Mater., 166 (2019) 87-91.

[65] B. Zhang, Q. B. Zheng, Z. D. Huang, S. W. Oh, J. K. Kim, SnO_2–graphene–carbon nanotube mixture for anode material with improved rate capacities, Carbon, 49 (2011) 4524-4534.

[66] Y. Sharma, N. Sharma, G. V. Subba Rao, B. V. R. Chowdari, Nanophase $ZnCo_2O_4$ as a High Performance Anode Material for Li-Ion Batteries, Adv. Funct. Mater., 17 (2007) 2855-2861.

[67] L. Zhou, K. Zhang, Z. Hu, Z. Tao, L. Mai, Y.-M. Kang, S.-L. Chou, J. Chen, Recent Developments on and Prospects for Electrode Materials with Hierarchical Structures for Lithium-Ion Batteries, Adv. Energy Mater., 8 (2018) 1701415.

[68] Y. Zhang, Y. Lu, S. Feng, D. Liu, Z. Ma, S. Wang, On-site evolution of ultrafine ZnO nanoparticles from hollow metal–organic frameworks for advanced lithium ion battery anodes, J. Mater. Chem. A, 5 (2017) 22512-22518.

[69] Q. Zhao, Y. Lu, J. Chen, Advanced Organic Electrode Materials for Rechargeable Sodium-Ion Batteries, Adv. Energy Mater., 7 (2017) 1601792.

[70] G.-L. Xu, Y. Li, T. Ma, Y. Ren, H.-H. Wang, L. Wang, J. Wen, D. Miller, K. Amine, Z. Chen, PEDOT-PSS coated ZnO/C hierarchical porous nanorods as ultralong-life anode material for lithium ion batteries, Nano Energy, 18 (2015) 253-264.

[71] L. Zeng, F. Xiao, J. Wang, S. Gao, X. Ding, M. Wei, ZnV_2O_4–CMK nanocomposite as an anode material for rechargeable lithium-ion batteries, J. Mater. Chem., 22 (2012) 14284-14288.

[72] X.-C. Zhao, P. Yang, L.-J. Yang, Y. Cheng, H.-Y. Chen, H. Liu, G. Wang, V. Murugadoss, S. Angaiah, Z. Guo, Enhanced Electrochemical Performance of Cu^{2+} doped TiO_2 Nanoparticles for Lithium-ion Battery, ES Mater. Manufacturing, 1 (2018) 67-71.

[73] Q. Fu, H. Cao, G. Liang, L. Luo, Y. Chen, V. Murugadoss, S. Wu, T. Ding, C. Lin, Z. Guo, A highly Li^+-conductive $HfNb_{24}O_{62}$ anode material for superior Li^+ storage, Chem. Commun., 56 (2020) 619-622.

[74] R. Li, X. Zhu, Q. Fu, G. Liang, Y. Chen, L. Luo, M. Dong, Q. Shao, C. Lin, R. Wei, Z. Guo, Nanosheet-based $Nb_{12}O_{29}$ hierarchical microspheres for enhanced lithium storage, Chem. Commun., 55 (2019) 2493-2496.

[75] P. Xie, Y. Li, Q. Hou, K. Sui, C. Liu, X. Fu, J. Zhang, V. Murugadoss, J. Fan, Y. Wang, R. Fan, Z. Guo, Tunneling-induced negative permittivity in Ni/MnO nanocomposites by a bio-gel derived strategy, Journal of Materials Chemistry C, 8 (2020) 3029-3039.

[76] S. S. Zhang, K. Xu, T. R. Jow, Electrochemical impedance study on the low temperature of Li-ion batteries, Electrochim. Acta, 49 (2004) 1057-1061.

[77] G. Liang, X. Sun, J. Lai, C. Wei, Y. Huang, H. Hu, J. Zou, Y. Xu, Asphalt-Decomposed Carbon-Coated SnO_2 as an Anode for Lithium Ion Batteries, J. Electron. Mater., 48 (2019) 3324-3329.

[78] T.-G. Kim, E. Samuel, B. Joshi, C.-W. Park, M.-W. Kim, M. T. Swihart, W. Y. Yoon, S. S. Yoon, Supersonically sprayed rGO−Zn_2SnO_4 composites as flexible, binder-free, scalable, and high-capacity lithium ion battery anodes, J. Alloys Compd., 766 (2018) 331-340.

[79] J. Huang, J. Wang, H. Zhong, L. Zhang, N-cyanoethyl polyethylenimine as a water-soluble binder for $LiFePO_4$ cathode in lithium-ion batteries, J. Mater. Sci., 53 (2018) 9690-9700.

[80] H. Cao, X. Xiao, X. Wang, J. Liu, P. Si, Morphology engineering of self-assembled porous zinc manganate hexagons for lithium ion storage, Electrochim. Acta, 330 (2020) 135260.